Journal of MATERIALS RESEARCH

Article
DOI:10.1557/s43578-021-00368-2

Phase relations and thermomechanical properties of $(Gd_2Zr_2O_7)_{1-x}(YbSZ)_x$ based thermal barrier coatings ($0 \le x \le 0.98$)

Mohadese Tabeshfar[1,2], Mehdi Salehi[1], Ghasem Dini[3], Jianying He[4], Mari-Ann Einarsrud[2], Kjell Wiik[2,a]

[1] Department of Materials Engineering, Isfahan University of Technology, 84156-83111 Isfahan, Iran
[2] Department of Materials Science and Engineering, NTNU Norwegian University of Science and Technology, Trondheim, Norway
[3] Department of Nanotechnology, Faculty of Chemistry, University of Isfahan, 81746-73441 Isfahan, Iran
[4] Department of Structural Engineering, NTNU Norwegian University of Science and Technology, 7491 Trondheim, Norway
[a] Address all correspondence to this author. e-mail: kjell.wiik@ntnu.no

Received: 4 February 2021; accepted: 25 August 2021; published online: 13 September 2021

Doped $Gd_2Zr_2O_7$ materials have interesting properties as thermal barrier coatings (TBC) to replace the YSZ topcoats traditionally used. Here we investigate the thermomechanical properties and phase relations of $Gd_2Zr_2O_7$ (GZO) alloyed with 5 mol% Yb_2O_3 stabilized ZrO_2 (YbSZ) in the composition range $(Gd_2Zr_2O_7)_{1-x}(YbSZ)_x$, $0 \le x \le 0.98$. With increasing YbSZ content, phase transformations from ordered to disordered pyrochlore to fluorite and tetragonal structures were observed. The thermal expansion coefficient (TEC) and Vickers hardness were correlated showing a maximum hardness (~ 11.5 GPa) and minimum TEC at $x = 0.82$. At 1000 °C, the TEC for the end members, $x = 0$ and 0.98, were 11.4 and 11.3 $\times 10^{-6}$ K^{-1}, respectively. The fracture toughness, K_{IC}, showed an average value around 1.5 MPa $m^{0.5}$ for $x \le 0.93$ and increased significantly at $x = 0.98$ reaching 5.4 MPa $m^{0.5}$ due to the presence of a ferroelastic phase. For TBC applications, compounds with $x = 0.98$ show promise due to high TEC and high K_{IC}.

Introduction

Thermal barrier coatings (TBCs) enhance the durability and energy efficiency of the hot section components of gas turbines. A TBC system typically consists of four main parts including a superalloy substrate, a metallic bond coat, a thermally grown oxide, and a ceramic topcoat [1–5]. The most common material used as the ceramic topcoat is 3.4–4.5 mol% yttria-stabilized zirconia (YSZ) [1, 2, 4, 6], applied either by electron beam physical vapor deposition (EBPVD) or atmospheric plasma spraying (APS). From a mechanical point of view, durability and failure mechanisms of TBCs are thoroughly described and discussed by Evans et al. [7] in their paper from 2001, and more details on failure due to hot corrosion, oxidation, erosion and thermal shock is reported in [8–12]. Of particular interest to aircraft engines is the ingestion of siliceous particulates (dust, sand, volcanic ash, runway debris) with the intake of air. At elevated temperature the finer debris tend to adhere to the coating surface and form calcium magnesium alumino-silicate (CMAS) and the TBCs may suffer from crack formation and delamination. The possible degradation of TBCs by molten CMAS deposits is extensively treated in the literature [13–15].

The state-of-the-art YSZ coating is mainly comprised of a non-transformable tetragonal (t') phase [16] that limits application to temperatures below 1200 °C, due to accelerated sintering and detrimental phase transformations at temperatures above 1200 °C [17–20].

In order to improve the efficiency of the gas turbines, the combustion temperature needs to be increased demanding replacements for YSZ. New thermal barrier oxide materials with higher stability, lower thermal conductivity, and improved sintering resistance at higher temperatures have attracted increasing attention [4, 21–24]. Rare-earth zirconates ($RE_2Zr_2O_7$) such as $La_2Zr_2O_7$, $Gd_2Zr_2O_7$, and $Sm_2Zr_2O_7$ have been considered to enhance the efficiency of TBCs [4, 21, 22, 25]. Among them, $Gd_2Zr_2O_7$ (GZO) has attracted extensive attention due to low thermal conductivity and enhanced phase stability [26–29]. However, the application of $Gd_2Zr_2O_7$ as the topcoat for TBCs is limited to a relatively short thermal cycling lifetime due to

low fracture toughness, K_{IC} [30–33]. To enhance the fracture toughness and thermal cycling lifetime of $Gd_2Zr_2O_7$ ceramics, considerable efforts have been made and there are several possible strategies to follow [27, 31, 34, 35].

There are two possible toughening mechanisms in zirconia-based materials [36]. The first mechanism is the well-established stress-induced phase transformation (transformation toughening) from the tetragonal (notation *t*) to monoclinic phase along the propagation of the crack [37]. The second mechanism is ferroelastic toughening due to the presence of a non-transformable tetragonal phase (notation *t′*) with ferroelastic properties [34, 38, 39]. Fracture energy is absorbed by ferroelastic domain switching in response to strain, and results in a significant enhancement in K_{IC} [34, 39]. The ferroelastic tetragonal phase is characterized by a tetragonality, $t' = c/a\sqrt{2}$ (a and c are the lattice parameters of the tetragonal structure), between 1.00 and 1.01 [40]. This toughening mechanism is also active at high temperatures, however it is lost above 1300 °C as the *t′*-phase converts to tetragonal *t*-phase and monoclinic phase on cooling from these high temperatures [19]. According to Zhao et al. [41] stress-induced order–disorder phase transformation along the crack propagation also represent a possible toughening mechanism, absorbing fracture energy along the path of the crack and resulting in enhanced K_{IC}.

Leckie et al. [42] showed that substitution of small ions into $Gd_2Zr_2O_7$ can be an effective strategy to improve the fracture toughness as well as the thermal expansion coefficient of $Gd_2Zr_2O_7$-based TBCs. Wang et al. [35] synthesized a series of Sc-substituted $Gd_2Zr_2O_7$ ceramics ($(Gd_{1-y}Sc_y)_2Zr_2O_7$, $0 \le y \le 0.2$) by chemical co-precipitation and reported that the Sc-substituted $Gd_2Zr_2O_7$ ceramics demonstrated an enhanced fracture toughness which could be attributed to the increased cohesive energy. They concluded that fracture toughness may also be enhanced by strengthening the bond energy between the atoms/ions in the crystal (cohesive or lattice energy) which is also affected by lattice distortion and structural disorder [35]. It is also reported that 3.5 mol% Yb_2O_3-stabilized ZrO_2 [34] and 3.5 mol% Er_2O_3-stabilized ZrO_2 [27] as toughening agents improved the fracture toughness of $Gd_2Zr_2O_7$ coatings due to the presence of the ferroelastic *t′* phase.

Cairney et al. [43] made a comparative study of the phase stability of ZrO_2 stabilized with Y and Yb, and reported that Yb offers enhanced *t′* phase stability compared with Y. Zhang et al. [34] synthesized 3.5 mol% RE_2O_3 (RE = Dy, Y, Er, Yb) stabilized ZrO_2 ceramics, and showed that ZrO_2 stabilized with 3.5 mol% Yb_2O_3 (YbSZ) exhibited the best phase-stability among these compounds. Feng et al. [44] reported the presence of the *t′* phase for ZrO_2 substituted with Yb_2O_3 in the interval from 3 to 6 mol% and that zirconia with 5 mol% Yb_2O_3 contained the highest amount of the *t′* phase and showed the best phase stability. There seems to be consensus that improved phase stability and higher fracture toughness are the main reasons for the longer thermal cyclic life of YbSZ among the rare earth oxide stabilized zirconia materials.

Zhang et al. [34] doped $Gd_2Zr_2O_7$ with 5 to 40 mol% of 3.5 mol% YbSZ to improve the fracture toughness and reported increased fracture toughness with increasing content of YbSZ and that the improvement was attributed to the *t′* phase.

In the present study we took advantage of results reported in [34, 43, 44] and explored the system $Gd_2Zr_2O_7$ (GZO) with 5 mol% Yb_2O_3 in ZrO_2 (YbSZ) corresponding to the nominal stoichiometry $(GZO)_{1-x}(YbSZ)_x$, and extended the range to include compositions from pure GZO to compositions with only 2 mol% GZO, corresponding to $0 \le x \le 0.98$.

The materials were sintered at 1600 °C and phase relations in the whole composition range were assessed by a combination of Raman and XRD. The objective of the study was to correlate thermomechanical properties such as TEC, hardness and fracture toughness with microstructure and phases (crystal structure) and identify compositions suitable for TBC applications.

Results

Characterization of GZO/YbSZ ceramic powders

The XRD pattern of the fabricated GZO powder shown in Fig. 1a confirms the formation of a single phase pyrochlore superstructure (PDF 00-016-0799) [45]. GZO with the pyrochlore structure has six Raman modes which are $A_{1g} + E_g + 4F_{2g}$ [46], while the Raman spectrum of defect fluorite structure only has one single broad band [47].

As shown in Fig. 1b, five Raman modes are observed confirming the presence of GZO with a pyrochlore structure [46]. Figure 2a shows the XRD pattern of the synthesized YbSZ powder confirming that Yb_2O_3 was completely dissolved in ZrO_2 and stabilized a single phase YbSZ with a tetragonal structure.

The Raman spectrum of the YbSZ powder presented in Fig. 2b shows the 6 Raman active modes corresponding to the formation of a tetragonal YbSZ phase [48]. Based on the lattice parameters calculated from the XRD pattern in Fig. 2a ($a = 3.6049$ Å, $c = 5.1346$ Å), $t = 1.0071$ hence confirming that the YbSZ powder has a *t′* tetragonal structure, consistent with results reported by Zhang et al. [34].

The XRD patterns of $(GZO)_{1-x}(YbSZ)_x$ with x between 0 and 0.98 and sintered at 1600 °C for 10 h are presented in Fig. 3a, while the phase distribution and lattice parameters are given in Table 1. Single phase materials are observed in the whole composition range except for sample F ($x = 0.93$) where both tetragonal and fluorite structure co-exist. The

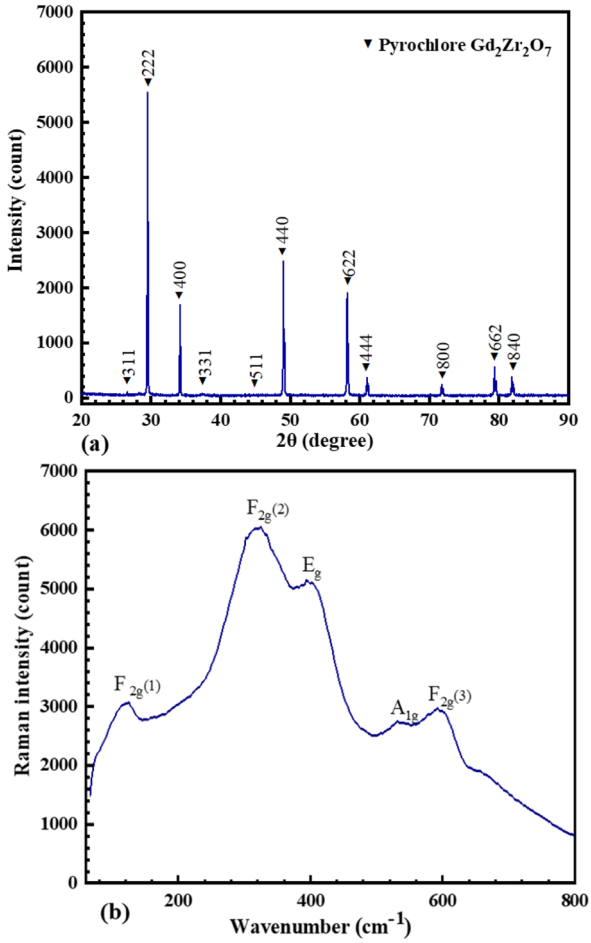

Figure 1: (a) XRD pattern of $Gd_2Zr_2O_7$ powder with Miller indices according to the pyrochlore superstructure [45] (PDF 00-016-0799) and (b) Raman spectrum of the $Gd_2Zr_2O_7$ powder showing five Raman modes (F_{2g} mode at ~ 125 cm^{-1}, F_{2g} mode at ~ 322 cm^{-1}, E_g at ~ 401 cm^{-1}, A_{1g} at ~ 537 cm^{-1} and F_{2g} at ~ 595 cm^{-1}) [46].

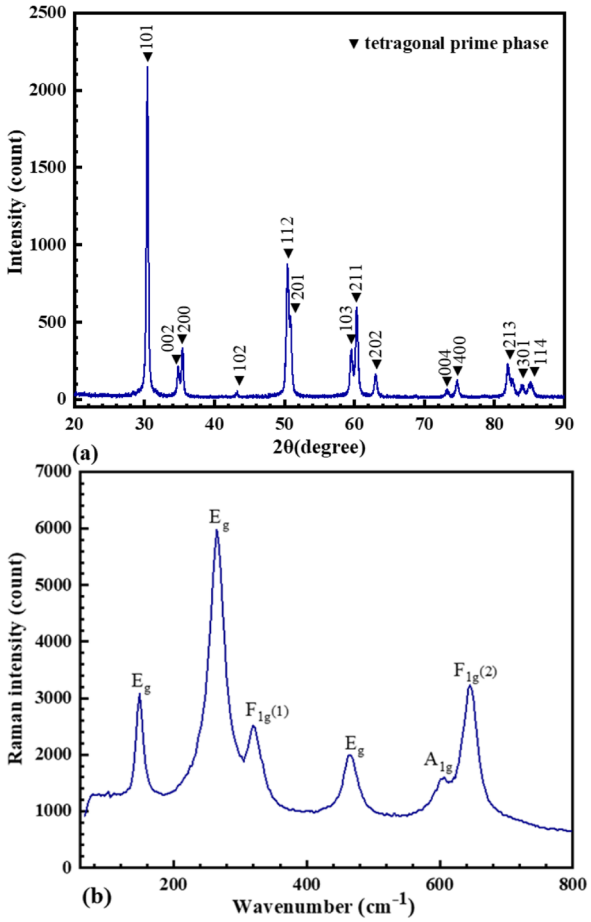

Figure 2: (a) XRD pattern of YbSZ powder confirming single phase with tetragonal structure (PDF 00-050-1089) and (b) Raman spectrum of the YbSZ powder.

tetragonality, t, of material G ($x = 0.98$) is at the border between t and t' phases, $t' = 0.010$. The diffraction lines are shifted toward higher 2θ with increasing YbSZ content (Fig. 3a), consistent with a decrease in lattice parameters.

According to [49], the pyrochlore structure is stable at $r(RE^{3+})/r(Zr^{4+})$ ratios between 1.46 to 1.78. Raman spectra proves crystallographic changes of GZO ceramics by increasing the YbSZ content (Fig. 3b). Raman spectroscopy is very sensitive to metal–oxygen vibrational modes, therefore a powerful tool to analyze the degree of local disorder [35].

The Raman line broadening is generally due to lattice strain and structural disorder [46] and from that perspective sample A represents an ordered pyrochlore while samples B and C are disordered pyrochlore structures (Fig. 3b and Table 1), inferred by the significant broadening of the Raman spectra observed for B and C. The interpretation is in accordance with Scheetz and White [50] reporting that line broadening in the zirconate pyrochlores is due to disorder. At even higher content of YbSZ, the structure changes to fluorite (sample D and E). The two weak Raman modes at 261 and 463 cm^{-1} observed for sample F indicate that both fluorite and tetragonal phases are co-existing. For sample G ($x = 0.98$) a well-defined tetragonal phase is evident.

Microstructure and mechanical properties of bulk GZO/YbSZ ceramic materials

Figure 4 shows the microstructure of the polished and thermally etched surfaces and values for density, porosity and grain size are included in Table 1. No secondary phases were observed in Fig. 4. The mean grain size increased with YbSZ content and reached a maximum of 15.1 µm for sample D ($x = 0.82$), and a further increase in YbSZ reduced the mean grain size to 1.8 µm (sample G, $x = 0.98$). The lowest porosity, 1%, was observed for pure $Gd_2Zr_2O_7$ (sample A) and a maximum porosity of almost 17% was observed for the sample with highest content of YbSZ (sample G, $x = 0.98$).

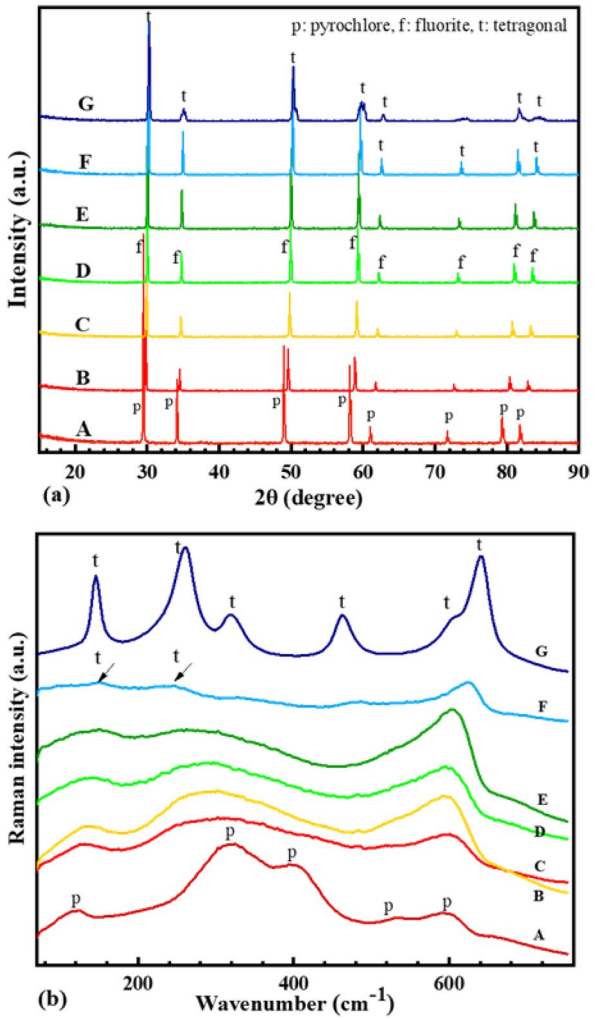

Figure 3: (a) XRD patterns and (b) Raman spectra of $(GZO)_{1-x}(YbSZ)_x$ (A: $x = 0$, B:$x = 0.60$, C: $x = 0.74$, D: $x = 0.82$, E: $x = 0.89$, F: $x = 0.93$, and G: $x = 0.98$) after sintering at 1600 °C for 10 h.

The hardness and fracture toughness of the fabricated ceramics are given in Fig. 5a. The hardness increases with increasing the YbSZ content up to $x = 0.74$ (sample C) and further addition of YbSZ gives a significant reduction in hardness reaching a minimum value of 6.7 GPa at $x = 0.98$ (sample G). A somewhat similar behavior is observed for the fracture toughness, K_{IC}, increasing from 1.3 (sample A) to 1.8 MPa $m^{0.5}$ at $x = 0.82$ (sample D). Sample D shows the highest fracture toughness among the samples with cubic structure (Table 1). A reduced fracture toughness is observed at even higher YbSZ content, reaching 1.4 MPa $m^{0.5}$ at $x = 0.93$ (sample F). A significant increase in fracture toughness is however observed for the sample with the highest content of YbSZ corresponding to 5.4 MPa $m^{0.5}$ at $x = 0.98$ (sample G). This enhanced fracture toughness coincides with the formation of a single-phase material with tetragonal structure (Table 1). It should be noted that sample G was loaded with 5 kg in order to generate cracks for assessment of K_{IC}, while the other samples were loaded with 300 g. SEM images of indented surfaces including crack formation for samples A and C are shown in Fig. 5b, c.

Elastic modulus (E) was assessed by nanoindentation and the results are given in Fig. 6a. Representative behavior of the force/displacement curves are presented in Fig. 6b for sample A. The values of the elastic modulus are rather constant from sample A to G, however the lowest value was measured for pure $Gd_2Zr_2O_7$ (sample A) whereas sample with x = 0.60 (sample B) reached the highest value at 225 GPa, indicating strengthening of the material by substitution of some Gd^{3+} with Yb^{3+}.

Thermal expansion coefficient of the bulk $(GZO)_{1-x}(YbSZ)_x$ ceramics

The variation in thermal expansion coefficient (TEC) with temperature provided in Fig. 7a shows an increasing TEC with temperature. Figure 7b shows the isothermal variation in TEC with composition at 200, 600 and 1000 °C and a parabolic behavior with respect to composition is evident at all isotherms and the TEC varies between 8.0 and 11.5×10^{-6} K^{-1}. The end members (sample A and G) display the highest TEC and the value for pure YbSZ, according to Guo et al. [51], is

TABLE 1: Density, porosity, grain size, lattice parameters and type of phase(s) present for the $(GZO)_{1-x}(YbSZ)_x$ samples after sintering at 1600 °C for 10 h.

Sample	x	YbSZ (wt%)	ρ_{bulk} (g cm^{-3})	ρ_{theor} (g cm^{-3})	$\rho_{\%}$ (%)	Porosity (%)	Grain size (μm)	Lattice param (Å)	Phase(s)
A	0	0	6.8 ± 0.06	6.9	99	1.0 ± 0.8	1.86 ± 0.6	10.530 (9)	Pyrochlore
B	0.60	25	6.6 ± 0.03	6.74	98	1.9 ± 0.5	8.4 ± 3.1	10.417 (3)	Disordered pyrochlore
C	0.74	37.5	6.5 ± 0.01	6.65	98	1.9 ± 0.2	10.4 ± 2.3	10.379 (1)	Disordered pyrochlore
D	0.82	50	6.4 ± 0.04	6.58	97	2.7 ± 0.6	15.1 ± 6.1	5.180 (4)	Fluorite
E	0.89	62.5	6.1 ± 0.08	6.53	94	5.8 ± 1.2	9.4 ± 3.7	5.168 (6)	Fluorite
F	0.93	75	5.9 ± 0.09	6.44	92	7.6 ± 1.4	7.3 ± 1.8	5.151 (6)	Fluorite + Tetragonal
G	0.98	90	5.3 ± 0.1	6.36	83	16.6 ± 2.3	1.8 ± 0.5	a:3.621 (8) c:5.171 (8)	Tetragonal (*t*)

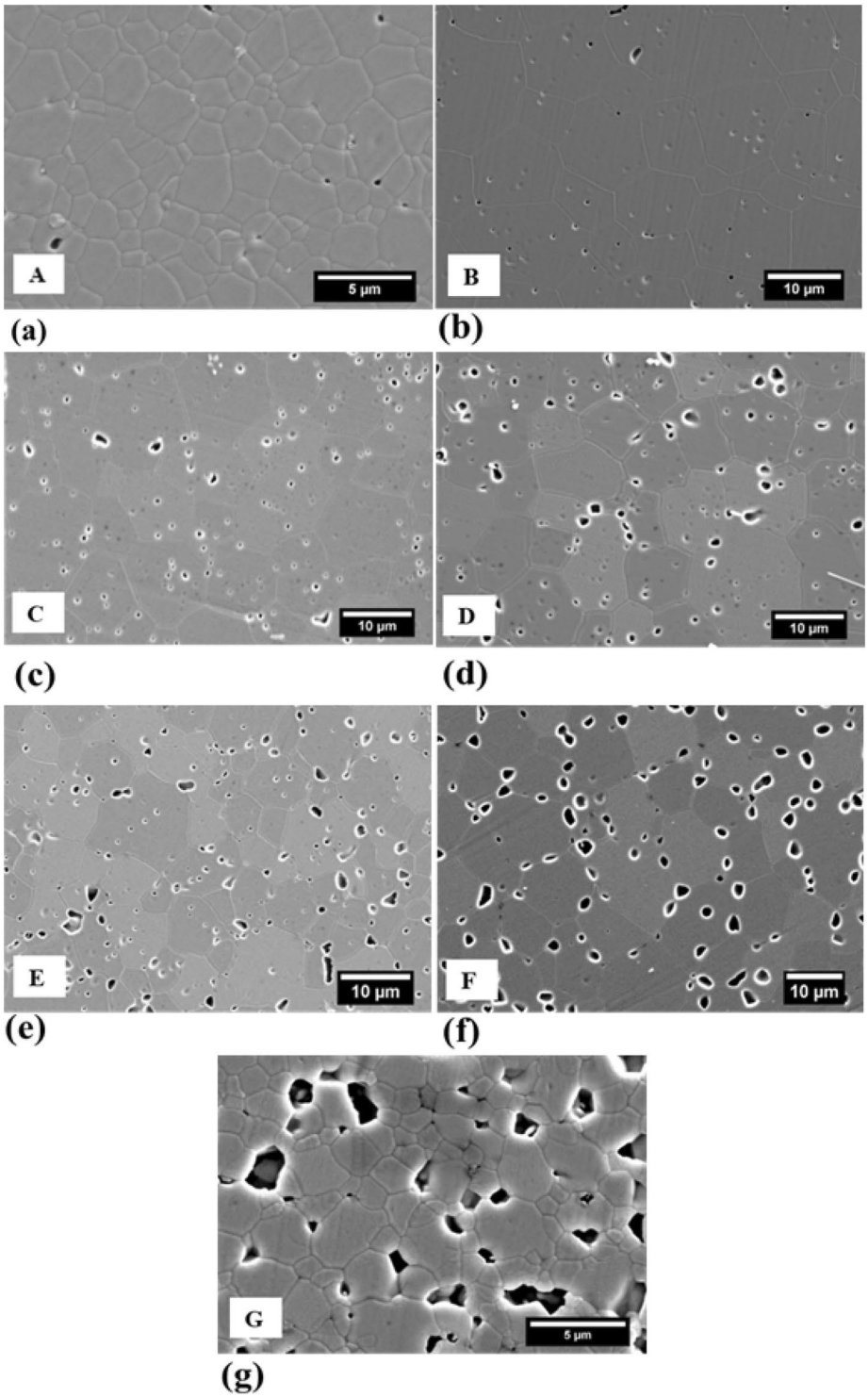

Figure 4: (a) to (g) the morphology of $(GZO)_{1-x}(YbSZ)_x$ samples from A (GZO) to G ($x = 0.98$) sintered at 1600 °C for 10 h.

11.25×10^{-6} K^{-1} at 1200 °C, which is in good agreement with the trend given in Fig. 7b. At low temperatures, sample G shows the highest TEC while at higher temperatures the thermal expansion coefficients of sample A and G are similar. A common reduction in TEC is observed for the alloyed samples with a minimum between $x = 0.82$ and 0.89 (sample D and E).

Discussion

Phase relations

Using a combination of XRD and Raman spectroscopy enabled to distinguish between ordered pyrochlore, disordered pyrochlore and fluorite phases in the $(GZO)_{1-x}(YbSZ)_x$ samples

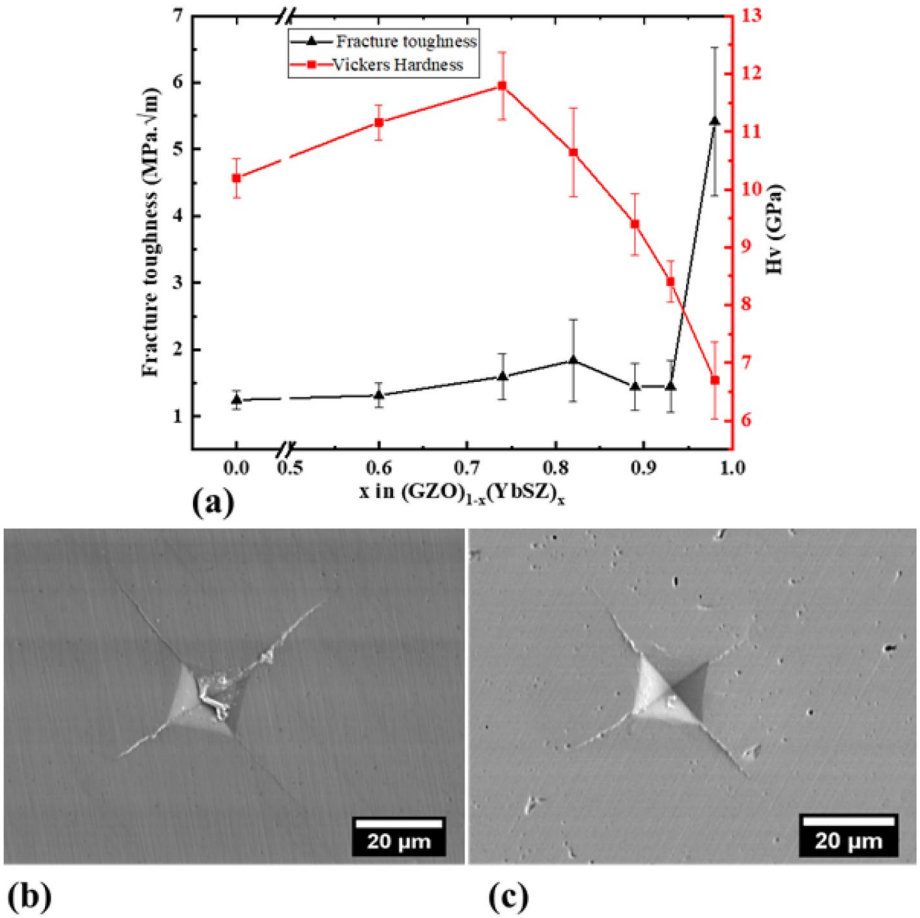

Figure 5: (a) Hardness and fracture toughness of the $(GZO)_{1-x}(YbSZ)_x$ samples, (b) and (c) SEM images of Vickers indents of sample A (left) and C (right), respectively (300 g load for 15 s).

[46–48]. With XRD, there are challenges in distinguishing between the fluorite (cubic) phase and the tetragonal phases due to the similarities in long range structure, however, these phases have distinguishable bands in their Raman spectra [52]. According to the phase study (Table 1), single phases are observed for x in the interval $0 \le x \le 0.89$ (Sample A to E) corresponding to solid solubility between GZO and YbSZ in this range. Both within the pyrochlore regime (Sample A to C) and the fluorite regime (Sample D to E) the lattice parameters decrease with increasing amount of YbSZ. This is anticipated to be due to the Gd^{3+} ions (ionic radius = 1.053 Å) being substituted by the smaller Yb^{3+} ions (ionic radius = 0.72 Å) [53, 54]. A two-phase regime occurs at $x = 0.93$ (Sample F) corresponding to the co-existence between a fluorite and a tetragonal phase. At even higher contents of YbSZ, $x = 0.98$ (Sample G), the tetragonal structure of YbSZ is seen to be preserved. All materials were sintered at 1600 °C expecting the tetragonal *t* phase to be stable, however for sample G ($x = 0.98$) the calculated tetragonality corresponded to a value at the border line between *t* and *t′*. The ternary phase diagram for the $Gd_2Zr_2O_7$–ZrO_2–Yb_2O_3 system is not reported in the literature. However, Fabrichnaya et al. [55] have investigated the phase equilibria in the $GdO_{1.5}$–ZrO_2–$YO_{1.5}$ system and presented ternary isothermal phase diagrams at temperatures between 1200 and 1600 °C. There are significant similarities between the present investigation and results reported by Fabrichnaya et al. However, in the ZrO_2-rich region they report a two-phase region corresponding to the coexistence between a fluorite structure and a tetragonal structure, as opposed to a single tetragonal phase observed in the present investigation (Sample G).

Microstructure

Increasing the YbSZ content from $x = 0$ to 0.82 (Sample A to D), densities between 99 and 97% are obtained (Table 1), showing good sinterability in this range. In the same composition range, there is also a monotonous increase in grain size from 1.9 to 15 μm. A closer inspection of the SEM micrographs in Fig. 4a–d shows an increasing number of trapped pores inside the grains with increasing grain size due to the enhanced rate of grain growth.

In the composition range from $x = 0.89$ to 0.98 (Table 1, sample E to G) the density is reduced from 94 to 83% at the same time as the average grain size is reduced from 9.4 to 1.8 μm, corresponding to a significant reduction in the sinterability with YbSZ content in this composition interval. The almost 10% reduction in density from sample F to G also

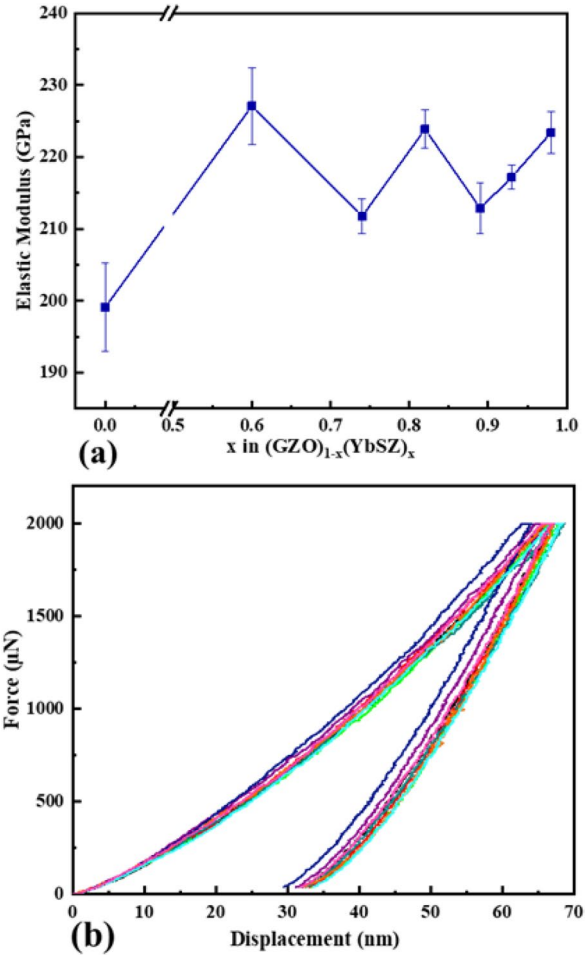

Figure 6: (a) Elastic modulus of all $(GZO)_{1-x}(YbSZ)_x$ samples (the lines are drawn as guide to the eye) and (b) nanoindentation load versus penetration depth curves for sample A.

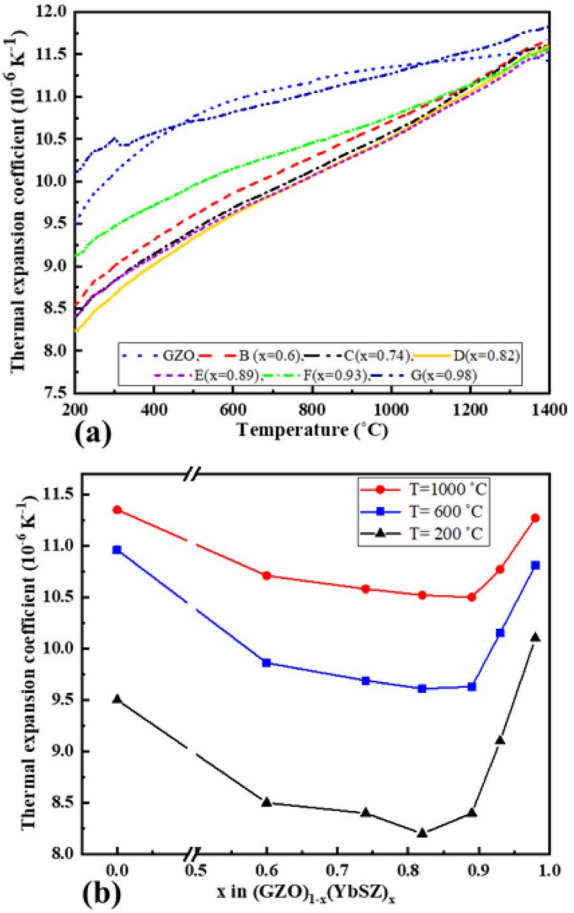

Figure 7: Thermal expansion coefficient (a) of the bulk $(GZO)_{1-x}(YbSZ)_x$ samples vs temperature and (b) of the bulk $(GZO)_{1-x}(YbSZ)_x$ ceramics at 200, 600 and 1000 °C.

coincides with the phase transition between fluorite/tetragonal to a single phase with tetragonal structure and indicate a significantly reduced densification rate for tetragonal structures due to the lower crystallographic symmetry and a lower number of independent diffusion paths for the cations. The concept of higher sinterability with decreasing melting point of the oxide [56] does not apply here since the melting point of $Gd_2Zr_2O_7$ (sample A) is somewhat higher than for GZO/YbSZ (Sample G).

From an application point of view the sintering properties are of importance. TBCs prone to progressively sinter at operating temperatures may lead to enhanced Young's modulus followed by delamination due to increased stress between TGO and TBC [57, 58]. Bakan et al. [31] investigated the relation between microstructure and failure in plasma sprayed GZO/YSZ and concluded that the presence of globular pores (and/or interlamellar cracks) enhance the performance of the TBC. The enhancement was explained by the reduced Young's modulus followed by less stress at the interfaces. This clearly shows that the sintering properties and resulting microstructure are important parameters with respect to the lifetime of TBCs at operating temperature. In the present investigation the aim was to obtain materials with as high density as possible and did not include attempts to design the microstructure.

Thermomechanical properties

Thermal expansion coefficient

Care should be taken when interpreting the change in TEC with composition, due to the simultaneous variation in phases. However, the simplest approach is to assume that the thermal expansion coefficient depends in general on the strength of the chemical bonds and will decrease with increasing bond strength. The variation in TEC at constant temperature shows a parabolic behavior with a minimum between $x = 0.82$ and 0.89 (Fig. 7b), indicating that the strongest bonds are around this composition. The high TEC values for the end members (sample A and G) also suggest that these compositions have the weakest bonds.

The average bond lengths are correlated with the strength of the bonds, corresponding to increased strength with reduced bond length. Assuming that there is a proportionality between average bond length and lattice parameter, the decreasing TEC for materials up to $x = 0.82$ correlate with a reduced lattice parameter (Table 1). However, the relation between lattice parameter and TEC is not so obvious for compositions with $x > 0.82$ and phase transitions between fluorite and tetragonal may also play a role. In addition, the anisotropic expansion of the tetragonal phase will also lead to strain in these structures as opposed to structures with cubic symmetry and may add to the TEC [59]. Overall, the TEC values are seen to vary between 8 and 11.5×10^{-6} K^{-1}, a somewhat expanded range compared to YSZ which typically vary between ~ 10 and 11×10^{-6} K^{-1} in the temperature range from 200 to 1000 °C [4].

Hardness

In general, the Vickers hardness should increase with average bond strength and as such correlate with the TECs. In Fig. 8, we compare the variation in TEC at 200 °C with Vickers hardness in the whole composition range. A correlation between TEC and hardness is seen, with a maximum in hardness close to the minimum in TEC and a reduction towards sample A and G.

Nano indentation

It was anticipated that the variation in the Young's modulus (Fig. 6a) would comply with TEC and hardness values, since there is a clear relation between strength and elastic modulus. However, except from an enhancement in elastic modulus in the interval from sample A to B, the variation in elastic modulus is scattered at even higher content of YbSZ. Based on the measurements we can conclude that the elastic modulus is enhanced by the addition of YbSZ, but the variation is partly in contradiction to TEC and hardness. Using the nanoindentation technique, only tiny volumes are indented, and the values are representative for very local area, even smaller than the individual grain in the materials, thus ruling out the effects of grain boundaries and pores. This may account for the lack of correlation between elastic modulus and TEC/hardness data.

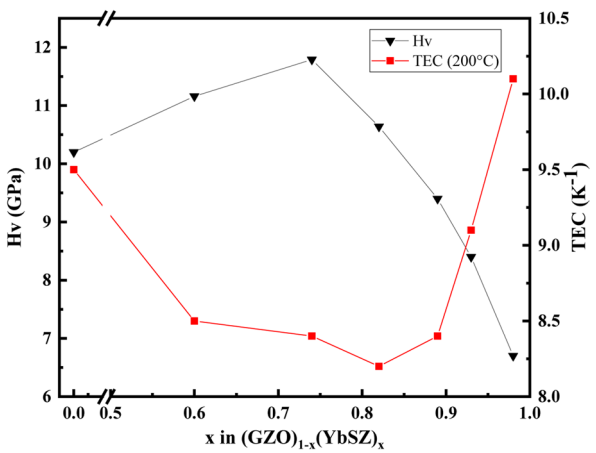

Figure 8: Comparison of thermal expansion coefficient (200 °C) and Vickers hardness of the bulk $(GZO)_{1-x}(YbSZ)_x$ samples.

Fracture toughness

It is well established that the fracture toughness decreases with increasing porosity for a single-phase material [60]. However, the fracture toughness also depends on several other parameters such as composition, structure and grain size as well as the presence of mechanisms able to enhance K_{IC} [7, 31, 56, 57, 61], which is why there is no simple relation between K_{IC} and porosity in this case (Fig. 5a and Table 1). Also, lattice distortion combined with strain and enhanced disorder will affect the fracture toughness. Wang et al. [35] claimed that the fracture toughness of ceramics was determined by the cohesive energy (bond strength) and showed that structural disorder and lattice distortion can enhance the cohesive energy. The measured fracture toughness in Fig. 5a correlates with the variation in TEC and hardness to a certain degree, with a maximum in toughness of 1.8 MPa $m^{0.5}$ at $x = 0.82$ (sample D) disregarding the high K_{IC} of sample G. The fracture toughness therefore correlates well with the variation in bonding energy (cohesive energy) in correspondence with [35]. However, the significantly enhanced fracture toughness observed for sample G ($x = 0.98$) of 5.4 MPa $m^{0.5}$ is surprising. This value approaches K_{IC} expected for transformation toughened PSZ (partially stabilized zirconia), where the toughening mechanism is due to the presence of a tetragonal phase embedded in a cubic phase followed by a tetragonal to monoclinic transition (volume expansion) at the crack tip. Since the material with $x = 0.98$ is confirmed to be a single phase with tetragonal structure, the transformation toughening mechanism is not likely to take place. A possible explanation of the enhanced fracture toughness is the presence of the ferroelastic tetragonal phase (t') although the sintering temperature was higher than the anticipated phase transition temperature between t' and t [17, 27]. An interesting follow up of this material would be a structural analysis in the vicinity of the crack. An improved thermal barrier coating (TBC) needs stable oxide materials with high TEC and high K_{IC}. From this perspective compositions with high content of YbSZ (around $x = 0.98$) will be preferred due to enhanced thermal expansion and fracture toughness. However, this composition is close to pure YbSZ and it is questionable whether this composition will exhibit similar low thermal conductivity as GZO enriched compositions.

Conclusion

$(GZO)_{1-x}(YbSZ)_x$ ceramics with x between 0 and 0.98 were successfully prepared. By a combination of XRD and Raman spectroscopy the phase relations were established showing the following phases with increasing x: Ordered pyrochlore ($x = 0$), disordered pyrochlore ($0.60 < x < 0.74$), fluorite ($0.82 < x < 0.89$), fluorite/tetragonal ($x = 0.93$) and tetragonal ($x = 0.98$). Vickers hardness and TEC were correlated showing a minimum in TEC and maximum in hardness (~ 11.5 GPa) at $x = 0.82$, reflecting the average bond strength of the compounds. At high temperatures (1000 °C) the TEC for the end members, $x = 0$ and 0.98, were 11.4 and 11. 3×10^{-6} K^{-1}, respectively. The variation in K_{IC} between $x = 0$ and 0.93 was small with an average value around 1.5 MPa $m^{0.5}$, however, with a significantly higher value of 5.4 MPa $m^{0.5}$ at $x = 0.98$. It is anticipated that the enhanced fracture toughness is due to the presence of a ferroelastic tetragonal phase (t'). The elastic modulus varied between 200 and 225 GPa for the different materials. No clear correlation between elastic modulus and TEC/hardness was observed. For application as thermal barrier coatings for gas turbines, compounds with high content of YbSZ (around $x = 0.98$) is preferred due to high TEC and high K_{IC}.

Materials and methods

Synthesis of GZO/YbSZ ceramics

5 mol% Yb_2O_3-stabilized ZrO_2 powder (YbSZ) was prepared by co-precipitation [34]. Yb_2O_3 (Wanfeng Adv. Materials Tech. Co., Ganzhou (Jiangxi), China; purity ≥ 99.998%) and $ZrOCl_2.8H_2O$ (Merck, Darmstadt, Germany; purity ≥ 99.0%) powders were selected as starting materials and appropriate amounts were dissolved in hot diluted nitric acid, and deionized water (molality of the solutions corresponding to 0.015 mol kg^{-1} and 0.31 mol kg^{-1}, respectively). The obtained solutions were subsequently mixed together under stirring to obtain a homogeneous solution. The resultant solution was added drop by drop to excess ammonia solution (pH > 12), and homogeneous gel-like precipitates were obtained. The precipitates were filtered and washed with distilled water and ethanol to pH 7 [27]. The obtained powder was dried at 110 °C for 18 h and subsequently calcined in air at 800 °C for 5 h.

The $Gd_2Zr_2O_7$ powder (GZO) was fabricated by the solid-state reaction method [62]. A mixture of Gd_2O_3 (Wanfeng Adv. Materials Tech. Co., Ganzhou (Jiangxi), China; purity ≥ 99.999%) and ZrO_2 (Sigma Aldrich, Taufkirchen, Germany, purity ≥ 99%, 5 μm) powders with a weight ratio of 1.47 was mechanically milled in a high energy planetary ball mill (Retsch PM100, Haan, Germany) using zirconia balls (15 mm diameter) in a polypropylene container, including ethanol, for 24 h. The amount of powder was around 20 g in each batch. The milled powder was heat treated in air at 1600 °C for 5 h (heating and cooling rates 200 °C h^{-1}).

Finally, the GZO with different amounts of YbSZ powder (Table 1) were mixed in a ball mill (zirconia balls and ethanol) at a speed of 250 rpm for 10 h. The obtained mixed powders were uniaxially pressed followed by cold isostatic pressing (CIP) at 200 MPa, and then reacted and sintered at 1600 °C in air for 10 h to make pellets for thermal and mechanical investigation. The samples are labelled from A to G, dependent on the amount of YbSZ. The dimension of the disc-shaped samples for mechanical measurements was 3 mm in height and 5 mm in diameter.

Characterization

The crystallographic structure and phase distribution of the powders and sintered samples were characterized by X-ray diffraction (XRD) (Bruker D8 DaVinci, (Billerica, Massachusetts, USA), using Cu Kα radiation and 2θ in the range from 20° to 90° at 0.02° s^{-1}. Raman spectra were recorded at the surface of the samples by a confocal Raman spectrometer (Witech, Alpha 300, Ulm, Germany) in a backscattering geometry with a spectral resolution of 1 cm^{-1} over a range from 100 to 3800 cm^{-1} with an excitation wavelength of 532 nm (frequency-doubled Nd-YAG laser operating at 66 mW power). For each sample, several Raman spectra were recorded at different positions at the sample surface to ascertain reproducible and representative results. Illumination and detection were performed through a microscope objective at ×50 magnification and a numerical aperture of 0.75. The microstructure of $(GZO)_{1-x}(YbSZ)_x$ sintered bulk samples was characterized by scanning electron microscopy (SEM) (Hitachi S-3400 N, Schaumburg, Illinois, USA) equipped with an energy dispersive X-ray spectrometer (EDS). The sintered samples were polished with a 1 μm alumina suspension, and thermally etched at 1500 °C for 0.5 h in air at cooling and heating rates of 400 °C h^{-1}. Grain size was measured by imageJ software. The thermal expansion coefficient (TEC) of samples was measured with a high-temperature dilatometer (Netzsch DIL 402C, Selb, Germany), from room temperature to 1400 °C in synthetic air using heating and cooling rates of 5 °C min^{-1}. The dimension of the samples for TEC measurements was 20 mm in length and 5 mm in diameter.

The Vickers hardness (H_V) of $(GZO)_{1-x}(YbSZ)_x$ pellets was measured using a microhardness tester (Zwick/Roell, ZHV30, Kennesaw, USA) at a load of 300 g for 15 s, apart from the sample with $x = 0.98$ which was subjected to a load of 5 kg. At least 10 valid indentations were made for each sample and an average value was reported. The fracture toughness (K_{IC}) was calculated based on the length of the cracks generated during indentation, using the following equation [35, 63]:

$$K_{IC} = 0.16\, H_V a^2 c^{-3/2} \quad (1)$$

where, a is the half-length of the indent diagonal, c is the half crack length measured from the middle of the indent to the tip of the crack.

The elastic modulus of the compounds was measured by nanoindentation [64] using a Hysitron Triboindenter 950 instrument (Minneapolis, MN USA) at room temperature equipped with a pyramidal Berkovich tip at a linear loading/unloading speed of 400 μN s^{-1}. Measurements were done in load control. The load–displacement history of the indentation was recorded for each sample, and the reported value was the average of at least 8 indentations.

Acknowledgments

Financial support from Iran National Science Foundation (INSF), Iranian Ministry of Science, Research and Technology (MSRT) and Department of Materials Science and Engineering (NTNU) is gratefully acknowledged.

Author contributions

MT: Investigation, writing original draft preparation, MS: Conceptualization, Methodology, Project administration, Supervision, Funding acquisition, Validation GD: Supervision, JH: Resources, MAE: Supervision, Writing—Review & Editing KW: Resources, Funding acquisition, Project administration, Supervision, Methodology, Writing—Review & Editing.

Funding

Open access funding provided by NTNU Norwegian University of Science and Technology (incl St. Olavs Hospital - Trondheim University Hospital).

Data availability

Data will be made available on reasonable request.

Declarations

Conflict of interest The authors declare that they have no conflict of interest.

Open Access

References

1. D.R. Clarke, M. Oechsner, N.P. Padture, Thermal-barrier coatings for more efficient gas-turbine engines. MRS Bull. **37**(10), 891–898 (2012). https://doi.org/10.1557/mrs.2012.232
2. R.A. Miller, Thermal barrier coatings for aircraft engines: history and directions. J. Therm. Spray Technol. **6**(1), 35 (1997). https://doi.org/10.1007/BF02646310
3. T.E. Strangman, Thermal barrier coatings for turbine airfoils. Thin Solid Films **127**(1/2), 93–105 (1985). https://doi.org/10.1016/0040-6090(85)90215-9
4. X.Q. Cao, R. Vassen, D. Stöver, Ceramic materials for thermal barrier coatings. J. Eur. Ceram. Soc. **24**(1), 1–10 (2004). https://doi.org/10.1016/S0955-2219(03)00129-8
5. A.S. Parlakyigit, D. Ozkan, M. Oge, Y. Ozgurluk, K.M. Doleker, T. Gulmez, A.C. Karaoglanli, Formation and growth behavior of TGO layer in TBCs with HVOF sprayed NiCr bond coat. Emerg. Mater. Res. **9**, 451–459 (2020). https://doi.org/10.1680/jemmr.18.00085
6. J.L. Smialek, R.A. Miller, Revisiting the birth of 7YSZ thermal barrier coatings: Stephan Stecura. Coatings **8**(7), 255 (2018). https://doi.org/10.3390/coatings8070255
7. A.G. Evans, D.R. Mumm, J.W. Hutchinson, G.H. Meier, F.S. Pettit, Mechanisms controlling the durability of thermal barrier coatings. Prog. Mater. Sci. **46**(5), 505–553 (2001). https://doi.org/10.1016/S0079-6425(00)00020-7
8. Y. Ozgurluk, K.M. Doleker, D. Ozkan, H. Ahlatci, A.C. Karaoglanli, Cyclic hot corrosion failure behaviors of EB-PVD TBC systems in the presence of sulfate and vanadate molten salts. Coatings **9**(3), 166 (2019). https://doi.org/10.3390/coatings9030166
9. Y. Ozgurluk, K.M. Doleker, A.C. Karaoglanli, Hot corrosion behavior of YSZ, $Gd_2Zr_2O_7$ and YSZ/$Gd_2Zr_2O_7$ thermal barrier coatings exposed to molten sulfate and vanadate salt. Appl. Surf. Sci **438**, 96–113 (2018). https://doi.org/10.1016/j.apsusc.2017.09.047
10. Y. Ozgurluk, K.M. Doleker, A.C. Karaoglanli, Investigation of the effect of V_2O_5 and Na_2SO_4 melted salts on thermal barrier coatings under cyclic conditions. Anti-Corros. Methods Mater. **644–650**, 2042 (2019). https://doi.org/10.1108/ACMM-12-2018-2042
11. A.C. Karaoglanli, Y. Ozgurluk, K.M. Doleker, Comparison of microstructure and oxidation behavior of CoNiCrAlY coatings produced by APS, SSAPS, D-gun HVOF and CGDS techniques. Vacuum **180**, 109609 (2020). https://doi.org/10.1016/j.vacuum.2020.109609

12. M. Kaplan, M. Uyaner, Y. Ozgurluk, K.M. Doleker, A.C. Karaoglanli: Evaluation of Hot Corrosion Behavior of APS and HVOF Sprayed Thermal Barrier Coatings (TBCs) Exposed to Molten Na_2SO_4+ V_2O_5 Salt at 1000° C, in *Engineering Design Applications* (Springer, 2019), pp. 441–459.
13. R.W. Jackson, E.M. Zaleski, B.T. Hazel, M.R. Begley, C.G. Levi, Response of molten silicate infiltrated $Gd_2Zr_2O_7$ thermal barrier coatings to temperature gradients. Acta Mater. **132**, 538–549 (2017). https://doi.org/10.1016/j.actamat.2017.03.081
14. S. Krämer, J. Yang, C.G. Levi, Infiltration-inhibiting reaction of gadolinium zirconate thermal barrier coatings with CMAS melts. J. Am. Ceram. Soc. **91**(2), 576–583 (2008). https://doi.org/10.1111/j.1551-2916.2007.02175.x
15. Y. Ozgurluk, K.M. Doleker, H. Ahlatci, A.C. Karaoglanli, Investigation of calcium–magnesium-alumino-silicate (CMAS) resistance and hot corrosion behavior of YSZ and $La_2Zr_2O_7$/YSZ thermal barrier coatings (TBCs) produced with CGDS method. Surf. Coat. Technol. **411**, 126969 (2021). https://doi.org/10.1016/j.surfcoat.2021.126969
16. I.R. Gibson, J.T.S. Irvine, Qualitative X-ray diffraction analysis of metastable tetragonal (t′) zirconia. J. Am. Ceram. Soc. **18**, 615–618 (2001). https://doi.org/10.1111/j.1151-2916.2001.tb00708.x
17. R.W. Trice, Y.J. Su, J.R. Mawdsley, K.T. Faber, A.R. De Arellano-Lopez, H. Wang, W.D. Porter, Effect of heat treatment on phase stability, microstructure, and thermal conductivity of plasma-sprayed YSZ. J. Mater. Sci. **37**(11), 2359–2365 (2002). https://doi.org/10.1023/A:1015310509520
18. M. Leoni, R.L. Jones, P. Scardi, Phase stability of scandia–yttria-stabilized zirconia TBCs. Surf. Coat. Technol. **108**, 107–113 (1998). https://doi.org/10.1016/S0257-8972(98)00617-3
19. K. Jiang, S. Liu, X. Wang, Phase stability and thermal conductivity of nanostructured tetragonal yttria–stabilized zirconia thermal barrier coatings deposited by air–plasma spraying. Ceram. Int. **43**(15), 12633–12640 (2017). https://doi.org/10.1016/j.ceramint.2017.06.142
20. S.A. Tsipas, Effect of dopants on the phase stability of zirconia-based plasma sprayed thermal barrier coatings. J. Eur. Ceram. Soc. **30**(1), 61–72 (2010). https://doi.org/10.1016/j.jeurceramsoc.2009.08.008
21. D. Stöver, G. Pracht, H. Lehmann, M. Dietrich, J.E. Döring, R. Vaßen, New material concepts for the next generation of plasma-sprayed thermal barrier coatings. J. Therm. Spray Technol. **13**(1), 76–83 (2004). https://doi.org/10.1007/s11666-004-0052-4
22. R. Vassen, X. Cao, F. Tietz, D. Basu, D. Stöver, Zirconates as new materials for thermal barrier coatings. J. Am. Ceram. Soc. **83**(8), 2023–2028 (2000). https://doi.org/10.1111/j.1151-2916.2000.tb01506.x
23. Z.G. Liu, J.H. Ouyang, Y. Zhou, J. Li, X.L. Xia, Densification, structure, and thermophysical properties of ytterbium-gadolinium zirconate ceramics. Int. J. Appl. Ceram. Technol. **6**(4), 485–491 (2009). https://doi.org/10.1111/j.1744-7402.2008.02289.x
24. R. Vaßen, F. Traeger, D. Stöver, New thermal barrier coatings based on pyrochlore/YSZ double-layer systems. Int. J. Appl. Ceram. Technol. **1**(4), 351–361 (2004). https://doi.org/10.1111/j.1744-7402.2004.tb00186.x
25. K.M. Doleker, Y. Ozgurluk, Y. Kahraman, A.C. Karaoglanli, Oxidation and hot corrosion resistance of HVOF/EB-PVD thermal barrier coating system. Surf. Coat. Technol. **409**, 126862 (2021). https://doi.org/10.1016/j.surfcoat.2021.126862
26. W. Pan, S.R. Phillpot, C. Wan, A. Chernatynskiy, Z. Qu, Low thermal conductivity oxides. MRS Bull. **37**(10), 917–922 (2012). https://doi.org/10.1557/mrs.2012.234
27. M. Li, L. Guo, F. Ye, Phase structure and thermal conductivities of Er_2O_3 stabilized ZrO_2 toughened $Gd_2Zr_2O_7$ ceramics for thermal barrier coatings. Ceram. Int. **42**(15), 16584–16588 (2016). https://doi.org/10.1016/j.ceramint.2016.07.079
28. K.M. Doleker, Y. Ozgurluk, H. Ahlatci, A.C. Karaoglanli, Evaluation of oxidation and thermal cyclic behavior of YSZ, $Gd_2Zr_2O_7$ and YSZ/$Gd_2Zr_2O_7$ TBCs. Surf. Coat. Technol. **371**, 262–275 (2019). https://doi.org/10.1016/j.surfcoat.2018.11.055
29. K.M. Doleker, O. Odabas, Y. Ozgurluk, H. Askerov, A.C. Karaoglanli, Effect of high temperature oxidation on Inconel 718 and Inconel 718/YSZ/$Gd_2Zr_2O_7$. Mater. Res. Express **6**(8), 86456 (2019). https://doi.org/10.1088/2053-1591/ab26d8
30. M.P. Schmitt, J.L. Stokes, B.L. Gorin, A.K. Rai, D. Zhu, T.J. Eden, D.E. Wolfe, Effect of Gd content on mechanical properties and erosion durability of sub-stoichiometric $Gd_2Zr_2O_7$. Surf. Coat. Technol. **313**, 177–183 (2017). https://doi.org/10.1016/j.surfcoat.2016.12.045
31. E. Bakan, D.E. Mack, G. Mauer, R. Mücke, R. Vaßen, Porosity–property relationships of plasma-sprayed $Gd_2Zr_2O_7$/YSZ thermal barrier coatings. J. Am. Ceram. Soc. **98**(8), 2647–2654 (2015). https://doi.org/10.1111/jace.13611
32. K.M. Doleker, A.C. Karaoglanli, Y. Ozgurluk, A. Kobayashi, Performance of single YSZ, $Gd_2Zr_2O_7$ and double-layered YSZ/$Gd_2Zr_2O_7$ thermal barrier coatings in isothermal oxidation test conditions. Vacuum **177**, 109401 (2020). https://doi.org/10.1016/j.vacuum.2020.109401
33. A.C. Karaoglanli, K.M. Doleker, Y. Ozgurluk, Interface failure behavior of yttria stabilized zirconia (YSZ), $La_2Zr_2O_7$, $Gd_2Zr_2O_7$, YSZ/$La_2Zr_2O_7$ and YSZ/$Gd_2Zr_2O_7$ thermal barrier coatings (TBCs) in thermal cyclic exposure. Mater. Charact. **159**, 110072 (2020). https://doi.org/10.1016/j.matchar.2019.110072
34. Y. Zhang, L. Guo, X. Zhao, C. Wang, F. Ye, Toughening effect of Yb_2O_3 stabilized ZrO_2 doped in $Gd_2Zr_2O_7$ ceramic for thermal barrier coatings. Mater. Sci. Eng. A **648**, 385–391 (2015). https://doi.org/10.1016/j.msea.2015.09.081
35. C. Wang, L. Guo, Y. Zhang, X. Zhao, F. Ye, Enhanced thermal expansion and fracture toughness of Sc_2O_3-doped $Gd_2Zr_2O_7$

ceramics. Ceram. Int. **41**(9), 10730–10735 (2015). https://doi.org/10.1016/j.ceramint.2015.05.008

36. B. Basu, Toughening of yttria-stabilised tetragonal zirconia ceramics. Int. Mater. Rev. **50**(4), 239–256 (2005). https://doi.org/10.1179/174328005X41113
37. R.H.J. Hannink, M.V. Swain, Progress in transformation toughening of ceramics. Annu. Rev. Mater. Sci. **24**(1), 359–408 (1994). https://doi.org/10.1146/annurev.ms.24.080194.002043
38. D. Baither, M. Bartsch, B. Baufeld, A. Tikhonovsky, A. Foitzik, M. Rühle, U. Messerschmidt, Ferroelastic and plastic deformation of t′-zirconia single crystals. J. Am. Ceram. Soc. **84**(8), 1755–1762 (2001). https://doi.org/10.1111/j.1151-2916.2001.tb00911.x
39. C. Mercer, J.R. Williams, D.R. Clarke, A.G. Evans, On a ferroelastic mechanism governing the toughness of metastable tetragonal-prime (t′) yttria-stabilized zirconia. Proc. R. Soc. A **463**(2081), 1393–1408 (2007). https://doi.org/10.1098/rspa.2007.1829
40. C. Viazzi, J.-P. Bonino, F. Ansart, A. Barnabé, Structural study of metastable tetragonal YSZ powders produced via a sol–gel route. J. Alloys Compd. **452**(2), 377–383 (2008). https://doi.org/10.1016/j.jallcom.2006.10.155
41. M. Zhao, X. Ren, W. Pan, Mechanical and thermal properties of simultaneously substituted pyrochlore compounds $(Ca_2Nb_2O_7)_x(Gd_2Zr_2O_7)_{1-x}$. J. Eur. Ceram. Soc. **35**(3), 1055–1061 (2015). https://doi.org/10.1016/j.jeurceramsoc.2014.10.009
42. R.M.R. Leckie: Fundamental issues regarding the implementation of gadolinium zirconate in thermal barrier systems. PhD-Thesis, *University of California, Santa Barbara,* (2006). https://www.proquest.com/docview/305349630
43. J.M. Cairney, N.R. Rebollo, M. Rühle, C.G. Levi, Phase stability of thermal barrier oxides: a comparative study of Y and Yb additions. Int. J. Mater. Res. **98**(12), 1177–1187 (2007). https://doi.org/10.3139/146.101595
44. J. Feng, X. Ren, X. Wang, R. Zhou, W. Pan, Thermal conductivity of ytterbia-stabilized zirconia. Scr. Mater. **66**(1), 41–44 (2012). https://doi.org/10.1016/j.scriptamat.2011.09.038
45. L. Ma, W. Ma, X. Sun, J. Liu, L. Ji, H. Song, Structure properties and sintering densification of $Gd_2Zr_2O_7$ nanoparticles prepared via different acid combustion methods. J. Rare Earths **33**(2), 195–201 (2015). https://doi.org/10.1016/S1002-0721(14)60402-6
46. J. Shi, Z. Qu, Q. Wang, Influence of temperature on the order-disorder transition in $Gd_2Zr_2O_7$. Key Eng. Mater. **697**, 386–389 (2016). https://doi.org/10.4028/www.scientific.net/kem.697.386
47. B.P. Mandal, N. Garg, S.M. Sharma, A.K. Tyagi, Solubility of ThO_2 in $Gd_2Zr_2O_7$ pyrochlore: XRD, SEM and Raman spectroscopic studies. J. Nucl. Mater. **392**(1), 95–99 (2009). https://doi.org/10.1016/j.jnucmat.2009.03.050
48. D. Gazzoli, G. Mattei, M. Valigi, Raman and X-ray investigations of the incorporation of Ca^{2+} and Cd^{2+} in the ZrO_2 structure. J. Raman Spectrosc. **38**(7), 824–831 (2007). https://doi.org/10.1002/jrs.1708
49. Y. Wu, L. Zheng, W. He, J. He, H. Guo, Effects of Yb^{3+} doping on phase structure, thermal conductivity and fracture toughness of $(Nd_{1-x}Yb_x)_2Zr_2O_7$. Ceram. Int. **45**(3), 3133–3139 (2019). https://doi.org/10.1016/j.ceramint.2018.10.213
50. B.E. Scheetz, W.B. White, Characterization of anion disorder in zirconate $A_2B_2O_7$ compounds by Raman spectroscopy. J. Am. Ceram. Soc. **62**(9–10), 468–470 (1979). https://doi.org/10.1111/j.1151-2916.1979.tb19107.x
51. L. Guo, C. Zhang, L. Xu, M. Li, Q. Wang, F. Ye, C. Dan, V. Ji, Effects of TiO_2 doping on the defect chemistry and thermophysical properties of Yb_2O_3 stabilized ZrO_2. J. Eur. Ceram. Soc. **37**(13), 4163–4169 (2017). https://doi.org/10.1016/j.jeurceramsoc.2017.04.065
52. M.R. Loghman-Estarki, R.S. Razavi, H. Edris, Synthesis and thermal stability of nontransformable tetragonal $(ZrO_2)_{0.96}(REO_{1.5})_{0.04}$ (RE=Sc^{3+}, Y^{3+}) nanocrystals. Defect Diffus. Forum. **334**(3), 60–64 (2013). https://doi.org/10.4028/www.scientific.net/DDF.334-335.60
53. R.D. Shannon, Revised effective ionic radii and systematic studies of interatomic distances in halides and chalcogenides. Acta Cryst. **32**(5), 751–767 (1976). https://doi.org/10.1107/S0567739476001551
54. L. Ma, W. Ma, X. Sun, L. Ji, J. Liu, K. Hang, Microstructures and mechanical properties of $Gd_2Zr_2O_7/ZrO_2$ (3Y) ceramics. J. Alloys Compd. **644**, 416–422 (2015). https://doi.org/10.1016/j.jallcom.2015.05.054
55. O. Fabrichnaya, C. Wang, M. Zinkevich, F. Aldinger, C.G. Levi, Phase equilibria and thermodynamic properties of the ZrO_2-$GdO_{1.5}$-$YO_{1.5}$ system. J. Phase Equilibria Diffus. **26**(6), 591–604 (2005). https://doi.org/10.1007/s11669-005-0004-9
56. Y. Zhang, J. Malzbender, D.E. Mack, M.O. Jarligo, X. Cao, Q. Li, R. Vaßen, D. Stöver, Mechanical properties of zirconia composite ceramics. Ceram. Int. **39**(7), 7595–7603 (2013). https://doi.org/10.1016/j.ceramint.2013.03.014
57. N.A. Fleck, A.C.F. Cocks, S. Lampenscherf, Thermal shock resistance of air plasma sprayed thermal barrier coatings. J. Eur. Ceram. Soc. **34**(11), 2687–2694 (2014). https://doi.org/10.1016/j.jeurceramsoc.2014.01.002
58. K.M. Doleker, Y. Ozgurluk, A.C. Karaoglanli, TGO growth and kinetic study of single and double layered TBC systems. Surf. Coat. Technol. **415**, 127135 (2021). https://doi.org/10.1016/j.surfcoat.2021.127135
59. T. Sheu, Anisotropic thermal expansion of tetragonal zirconia polycrystals. J. Am. Ceram. Soc. **76**(7), 1772–1776 (1993). https://doi.org/10.1111/j.1151-2916.1993.tb06646.x
60. J.-D. Lin, J.-G. Duh, Fracture toughness and hardness of ceria- and yttria-doped tetragonal zirconia ceramics. Mater. Chem. Phys. **78**(1), 253–261 (2003). https://doi.org/10.1016/S0254-0584(02)00327-9

61. E.M. Donohue, N.R. Philips, M.R. Begley, C.G. Levi, Thermal barrier coating toughness: measurement and identification of a bridging mechanism enabled by segmented microstructure. Mater. Sci. Eng. A **564**, 324–330 (2013). https://doi.org/10.1016/j.msea.2012.11.126
62. D. Lee, T.W. Kim, K.S. Lee, Design of thermal barrier coatings using gadolinium zirconate ceramics: a study on gadolinium zirconate/YSZ bilayers. J. Ceram. Soc. JAPAN **117**(1365), 550–554 (2009). https://doi.org/10.2109/jcersj2.117.550
63. A.G. Evans, E.A. Charles, Fracture toughness determinations by indentation. J. Am. Ceram. Soc. **59**(7–8), 371–372 (1976). https://doi.org/10.1111/j.1151-2916.1976.tb10991.x
64. L. Kurpaska, J. Jagielski, Mechanical properties of irradiated $Gd_2Zr_2O_7$ pyrochlores as studied by nanoindentation technique—effect of grains and grain boundaries. Nucl. Instruments Methods Phys. Res. Sect. B **379**, 107–111 (2016). https://doi.org/10.1016/j.nimb.2016.04.032